

An accurate analytical model for squirt flow in anisotropic porous rocks — Part 2: Complex geometry

Yury Alkhimenkov¹ and Beatriz Quintal¹

ABSTRACT

Seismic waves exhibit strong attenuation and velocity dispersion when they propagate in porous rocks saturated with a fluid. The main cause of such energy dissipation is fluid flow in the pore space, so called squirt flow. Squirt flow takes place between interconnected pores and cracks or grain-to-grain contacts. The corresponding theory can be used to characterize porous rocks in the subsurface with noninvasive seismic methods. We extend the analytical model for a classical pore geometry presented in part 1 of our paper to more complex geometries of the pore space, where the crack edge is partially connected to multiple pores. This pore geometry is much more closely representative of rocks than the classical geometry where the crack edge is fully connected to a toroidal pore. We develop an approach to calculate the model compliance taking into account the interconnectivity

of the crack and pores. We redefine a squirt flow length parameter which takes into account the geometrical configuration of the multiple connections between a crack and the surrounding pores. This configuration will control the geometrical flow pattern and thus the diffusion length scale or, in other words, the characteristic frequency. We validate our analytical model against inherently accurate 3D numerical solutions. The analytical and numerical results are in excellent agreement for a range of different pore geometries. Published analytical solutions expect the user to know the dry stiffness (e.g., from laboratory measurements), but in our work, we also provide a way to calculate analytically the dry stiffness for the precise geometry that we consider. The new analytical model redefines the quantitative and qualitative description of seismic attenuation and velocity dispersion due to squirt flow. We provide the MATLAB and symbolic Maple routines to reproduce our main results.

INTRODUCTION

A passing seismic wave causes small deformations in rocks. Because rocks are heterogeneous at all scales, such deformations cause a heterogeneous strain field distribution in the rock. If a rock is fluid saturated, the heterogeneous strain field causes fluid flow until the fluid pressure equilibrates (Müller et al., 2010). Fluid flow can take place at different scales; at the pore scale, it is called the squirt flow and is known to cause strong wave energy dissipation and velocity dispersion. Many analytical models have been suggested to quantify the squirt flow effects on propagating waves, e.g., squirt flow between interconnected cracks (Mavko and Nur, 1975; O'Connell and Budiansky, 1977; Palmer and Traviolia, 1980), between interconnected compliant cracks and stiff pores (Murphy et al., 1986; Mukerji and Mavko, 1994; Dvorkin et al., 1995; Pride et al., 2004; Gurevich et al., 2010), and between interconnected small aspect ratio cracks and

spheroidal pores (Xu, 1998; Chapman et al., 2002; Chapman, 2003; Jakobsen and Chapman, 2009). In real rocks, examples of compliant pores having small aspect ratios are microcracks and grain contacts.

Several numerical approaches have been proposed to study squirt flow (Zhang et al., 2010; Zhang and Toksöz, 2012; Quintal et al., 2016, 2019; Das et al., 2019). Based on the approach proposed by Quintal et al. (2019), several 3D numerical studies have been conducted for several pore space geometries (Alkhimenkov et al., 2020a, 2020b; Lissa et al., 2020). Lissa et al. (2021) study frequency-dependent attenuation caused by squirt flow in a pore geometry of a real rock derived from 3D images based on the microcomputed X-ray tomography. Alkhimenkov et al. (2020a) compare accurate numerical solutions against a published analytical model for squirt flow (Collet and Gurevich, 2016) for the exact same classical pore geometry and show that significant discrepancies exist. The classical pore geometry consists of a penny-shaped

Manuscript received by the Editor 23 March 2022; revised manuscript received 4 August 2022; published ahead of production 12 September 2022; published online 6 October 2022.

¹University of Lausanne, Institute of Earth Sciences, Lausanne, Switzerland and University of Lausanne, Swiss Geocomputing Centre, Lausanne, Switzerland.
E-mail: yury.alkhimenkov@unil.ch (corresponding author); beatriz.quintal@unil.ch.

© 2022 Society of Exploration Geophysicists. All rights reserved.

(circular) crack fully connected to a surrounding toroidal stiff pore. Recently, Alkhimenkov and Quintal (2021), in part I of this study, propose a new analytical model which is in a good agreement with an accurate 3D numerical simulation for the classical pore geometry.

In this contribution, we first improve the accuracy of the analytical model presented in part I (Alkhimenkov and Quintal, 2021). Then, we extend the analytical model presented in part I (Alkhimenkov and Quintal, 2021) to more complex geometries of the pore space, where the crack is only partially connected to one or more spherical pores. For that, we propose a new approach to calculate the model compliances for more complex geometries. We show that the fluid flow directions and, consequently, the characteristic frequency change dramatically compared with what happens in the classical pore geometry. To take this into account, we present a new parameter to characterize the characteristic frequency. We also derive another solution for the crack stiffness relaxation. We validate all the results against accurate 3D numerical solutions based on the exact same model geometry. We provide MATLAB and symbolic Maple routines to allow the reader to reproduce our main results and/or to obtain results for other material properties and pore sizes (Alkhimenkov and Quintal, 2021).

NUMERICAL ANALYSIS

For the numerical analysis, we explore several 3D numerical models consisting of a pore space saturated with a fluid and embedded in an elastic solid grain material. The numerical method is described in Quintal et al. (2019). The solid grains are described as a linear isotropic elastic material and the fluid phase is described by the quasi-static linearized compressible Navier-Stokes momentum equation. To obtain all components of the stiffness matrix C_{ij} (Voigt notation), we perform direct relaxation tests by applying a displacement boundary condition of the form $u = 10^{-8} \times \exp(i\omega t)$ to a certain external wall of the model, where $\omega = 2\pi f$ is the angular frequency, f is the frequency, t is the time, and i is the imaginary unit (Figure 1). A detailed description of the applied boundary conditions is given in Alkhimenkov et al. (2020a, 2020b). The models considered here are as follows:

- 1) A model with a crack connected to fractions of a torus (crack aspect ratio $\alpha = 0.02$).
- 2) A model with a crack connected to spherical pores (crack aspect ratio $\alpha = 0.01$).

The material parameters used in all models are shown in Table 1. The elastic solid grain material is represented by a rectangular cuboid with the dimensions of 0.4 m \times 0.4 m \times 0.2 m in all simula-

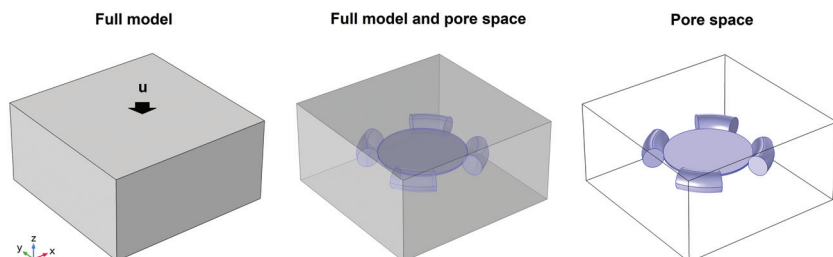


Figure 1. Sketch illustrating the model geometry of a crack connected to fractions of a torus. The displacement boundary condition $u = 10^{-8} \times \exp(i\omega t)$ is applied to the top boundary of the model to calculate the C_{33} component of the effective stiffness matrix (Voigt notation).

tions. The geometric properties of the pore space are given in the corresponding sections. The geometry in all models is scalable; i.e., the numerical solution remains unchanged if all the geometrical properties are rescaled by any fraction. An illustration of the model with a crack connected to fractions amounting to 4/9 of a torus is shown in Figure 1.

Fractions of a torus

In part I (Alkhimenkov et al., 2020a), we perform a 3D numerical study to compute the stiffness moduli dispersion and attenuation due to squirt flow for a classical geometry, where a crack (flat cylinder) connected to a toroidal pore. The numerical results of the effective stiffness modulus $[C_{33}^*(\omega)]_{\text{sat}}$ (Voigt notation) show that the slopes of the high-frequency asymptote of the attenuation curve are proportional to $\approx \omega^{-4/10}$, whereas a published analytical model (Collet and Gurevich, 2016) suggests $\approx \omega^{-1}$. Note that, in part I, we propose that the attenuation curve is proportional to $\approx \omega^{-1/2}$, which is indeed a good approximation and allowed us to provide simple closed-form expressions of the analytical model. However, the reason for such an asymptote of the attenuation curve ($\approx \omega^{-4/10}$) has remained unexplored. To further investigate the shape of the dimensionless attenuation $1/Q$ for different geometries, we present the results for a crack connected to different fractions of a torus (Figure 2). They include the fluid pressure snapshots at different frequencies (low frequency — 10 Hz, high frequency — 5.6×10^6 Hz, and the characteristic frequency) and the real part of the $[C_{33}^*(\omega)]_{\text{sat}}$ complex-valued component of the stiffness matrix and the dimensionless attenuation ($1/Q$). The geometrical properties of the model with crack aspect ratio $\alpha = 0.02$ are shown in Table 2. Figure 2 provides us with several insights into the physics of squirt flow and the shape of the attenuation and dispersion curves, as described next. The fluid pressure snapshots of a model at three different frequencies (Figure 2b–2f) help us to better understand the physics of squirt flow. The fluid pressure snapshots of a model corresponding to the configuration where a zero fluid pressure boundary condition (Figure 2a) is applied to the edge of the crack (representing a pore having an infinite volume while the pore is absent) are shown for comparison (Alkhimenkov et al., 2020a).

Low-frequency limit

At low frequencies, the fluid pressure is low and uniform in all the models representing the so-called relaxed state (Figure 2a–2f). One can observe that the fluid pressure at the low frequency is the highest for the 1/9 torus model (Figure 2b), the fluid pressure magnitude is reducing as the volume of the pore is increasing (Figure 2c–2f) and is the lowest for the $P_f = 0$ model. In other words, the volume of the stiff pore acts as a “storage volume” for the fluid pressure diffusion from the crack. This trend shows that the volume of the stiff pore has a significant impact on the overall attenuation magnitude, as shown in Figure 2h.

The characteristic frequency

At the characteristic frequency, the fluid pressure is high at the center of the crack but low close to the edge of the crack. This configuration corresponds to the maximum gradients of the

fluid pressure in the crack. Thus, the crack stiffness is high at the crack center but low at the edge, except for the 1/9 torus model, where the crack stiffness is high at the crack edge opposite to the pore. The transition from the low-frequency limit to the characteristic frequency is approximately the same in all the models (Figure 2a–2f), that is why the behavior of the attenuation curve $1/Q$ and its asymptote is the same in all models for frequencies below the characteristic frequency (Figure 2h).

High-frequency limit

At high frequencies, the fluid pressure snapshots are different in all the models (Figure 2a–2f) as well as the shapes of the attenuation curves $1/Q$ (Figure 2h). One can observe a region of a high fluid pressure close to partially connected pores, which are indicated as

Table 1. Material properties used in all models.

Material parameter	Solid	Fluid
Solid bulk modulus K (GPa)	36	4.3
Solid shear modulus μ (GPa)	44	0
Fluid shear viscosity η (Pa · s)	0	1.414

“anomaly” in Figure 2b–2f. For the big torus model, the fluid pressure anomaly is present along the whole circumference (“red ring” in Figure 2f). However, there is no such anomaly in the $P_f = 0$ model (high frequency in Figure 2a), explaining why this model is in agreement with the analytical model of Collet and Gurevich (2016) and Alkhimenkov et al. (2020a). These high pressure anomalies are

Table 2. Geometric properties for the big pore model, which is the model where the crack is connected to a toroidal pore.

Geometric parameter	Big pore model
Flat cylinder (crack) radius b (m)	0.1
Flat cylinder (crack) thickness h (m)	0.004
Crack aspect ratio $\alpha = h/(2b)$	0.02
Major radius of torus $b + r$ (m)	0.124
Minor radius of torus r (m)	0.024
Total porosity	≈ 0.0478
Crack porosity	≈ 0.0039

Major radius — the distance from the center of the tube to the center of the torus. Minor radius — the radius of the tube (our isometric pore). The volume of the fractions of the torus correspond to 1/9, 4/9, 6/9, and 8/9 of the torus volume.

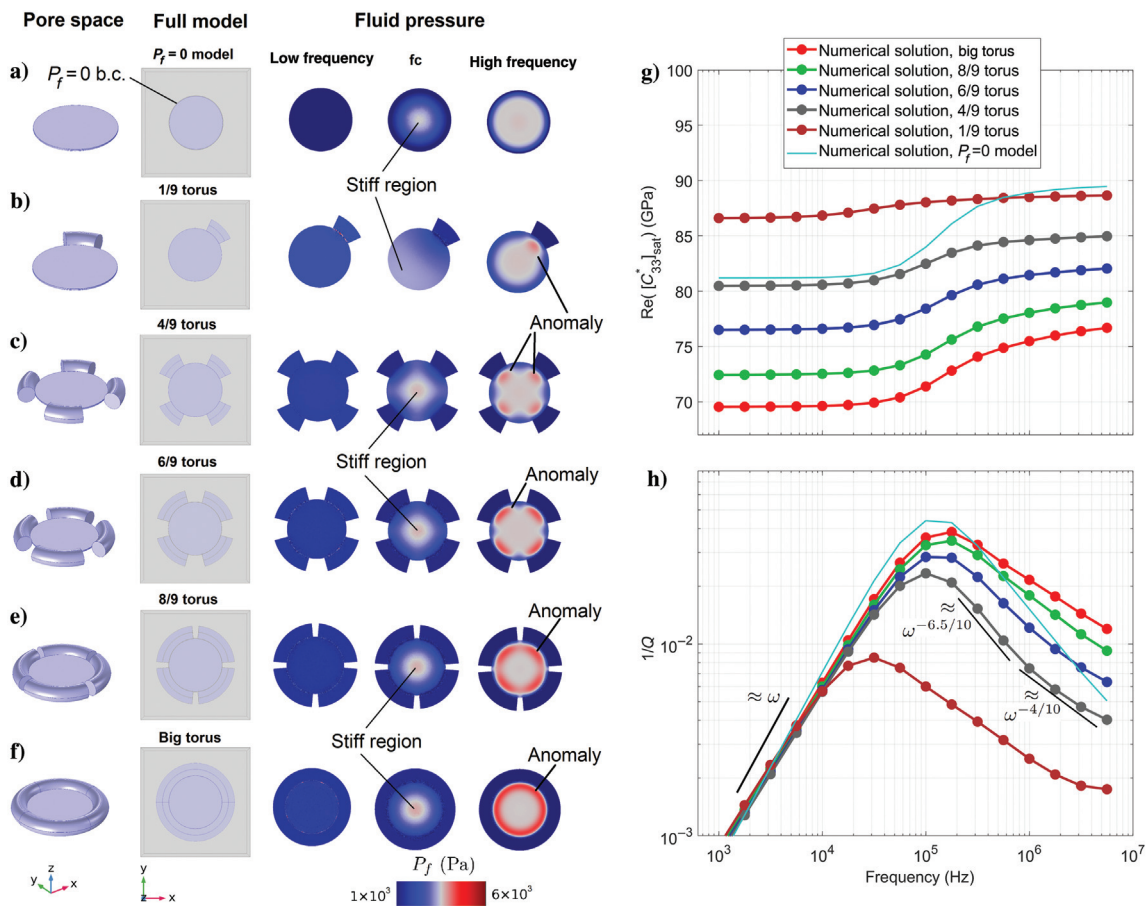


Figure 2. (a) The $P_f = 0$ model, (b) 1/9 torus model, (c) 4/9 torus model, (d) 6/9 torus model, (e) 8/9 torus model, and (f) the big pore model. Results of numerical simulations for (g) the real part of the C_{33} component and (h) corresponding dimensionless attenuation. The crack aspect ratio is $\alpha = 0.02$.

Downloaded 10/07/22 to 185.25.195.104. Redistribution subject to SEG license or copyright; see Terms of Use at http://library.seg.org/page/policies/terms DOI:10.1190/geo2022-0143.1

responsible for different shapes of the attenuation curves $1/Q$ at high frequencies in the considered models (Figure 2h).

The characteristic frequency is shifted to lower values as the fraction of the torus is reduced (Figure 2h). However, the characteristic frequency of the $1/9$ torus model is approximately one order of magnitude lower compared with the model with the full torus. Note that the crack aspect ratio is the same in all simulations which means that the crack aspect ratio does not control the characteristic frequency of squirt flow as it was believed until now. Instead, a different parameter controls the characteristic frequency, which is explored in the next sections.

Spherical pores

To further understand which parameters control the characteristic frequency f_c of squirt flow and to what extent the pore shape affects the shape of the dispersion and attenuation curves, we present numerical results for models with a crack partially connected to spherical pores in comparison with that of a crack fully connected with a torus (Figure 3). The geometrical properties of this set of models with crack aspect ratio $\alpha = 0.01$ are shown in Table 3.

Low-frequency limit

At low frequencies, the fluid pressure is low and uniform in all the models (Figure 3a–3d) similar to the model with a crack connected to fractions of the torus (Figure 2). The fluid pressure magnitude is the lowest in the four spheres model (Figure 2b) and increases in the models with one and two spheres (Figure 2c and 2d). Obviously, the model with four spheres has the largest volume of stiff pores compared with other models; thus, there is sufficient volume to store the

fluid flowing from the crack resulting in low fluid pressure. The big pore model with crack aspect ratio $\alpha = 0.01$ has approximately the same volume of the stiff pores as the model with two spheres; however, the attenuation peak (and the cumulative attenuation) of the big pore model is the greatest among other models. This means that the volume of the stiff pores and the model compliances are the key parameters determining the attenuation magnitudes. The difference between the dry moduli of the interconnected crack and pore and the moduli of the interconnected dry pore and saturated crack (i.e., modified frame) defines the attenuation magnitude. This difference is the largest for the big pore model, which is why the attenuation also is the largest. The volume of the stiff pores is another important parameter, which controls the attenuation magnitude — the volume should be sufficiently large, two orders of magnitude larger than the crack volume (Alkhimenkov et al., 2020a), to keep the fluid pressure low in the pore at low frequencies.

The characteristic frequency

At the characteristic frequency, the fluid pressure is high at the center of the crack (Figure 3) similar to the previous models (Figure 2). The shape of the central region of the high fluid pressure in the crack is slightly different in all models. Nevertheless, the shape of the attenuation curve $1/Q$ at low frequencies is the same in all models (Figure 3f).

High-frequency limit

At high frequencies, the fluid pressure snapshots (Figure 3a–3d) and the shape of the attenuation curve $1/Q$ (Figure 3f) exhibit similar behavior compared with that of the fraction of the torus models

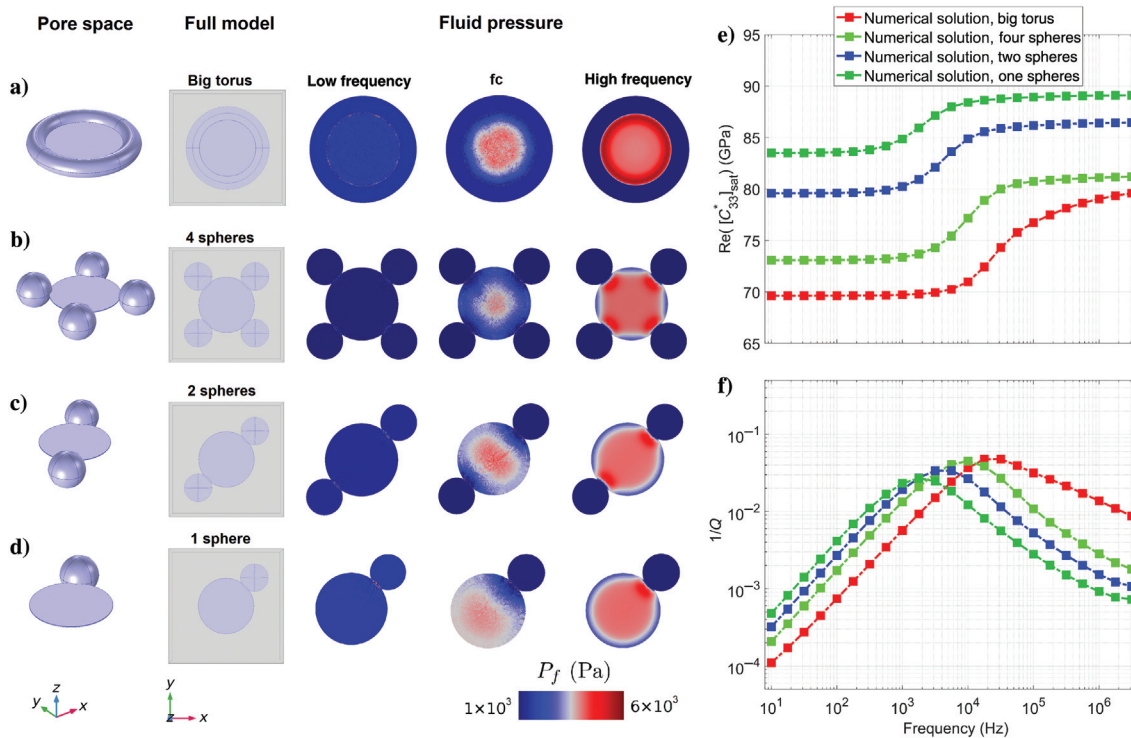


Figure 3. (a) The big pore model and the models with (b) four spheres, (c) two spheres, and (d) one sphere. Results of numerical simulations for (e) the real part of the C_{33} component and (f) corresponding dimensionless attenuation. The crack aspect ratio is $\alpha = 0.01$.

(Figure 2f). The shape of the attenuation curve of the big pore model with $\alpha = 0.01$ (Figure 3a–3f) is the same as in the big torus model with $\alpha = 0.02$ (Figure 2h); the “ring” anomaly of fluid pressure at high frequencies also is similar. The anomalies of high fluid pressure at high frequencies due to the connectivity with spheres (Figure 3a–3d) exhibit similar behavior as in the models with fractions of the torus (Figure 2). The high pressure anomalies also are similar to those presented for the models with a crack connected to fractions of the torus (Figure 2).

The characteristic frequency is shifted to lower values as the connected portion of the crack circumference is reduced. This portion is equal to the whole crack circumference for the big pore model, is lower for the models with spherical pores, and is the lowest for the one sphere model.

ANALYTICAL MODEL

Here, we extend the analytical model presented in part 1 (Alkhimenkov and Quintal, 2021) to the geometries involving cracks which are partially connected to one or multiple stiff pores. In addition, we improve the accuracy of the high-frequency regime of the analytical model presented in part 1 (Alkhimenkov and Quintal, 2021). The workflow is similar to part 1; however, we provide more general approaches to calculate dry model compliances and the crack stiffness relaxation functions. For consistency, we present the workflow in a similar way as was done in part 1 (Figure 4).

- 1) First, we calculate (or measure) the moduli of the dry rock (step 1 in Figure 4). We need the moduli of the dry model with interconnected pore and crack as well as the moduli of the same model but with the crack normal compliance equal to zero (or equal to a small number for the finite thickness crack).
- 2) Second, we calculate the crack stiffness relaxation function due to squirt flow and use that expression as the frequency-dependent crack stiffness. As a result, we obtain the frequency-dependent moduli of the modified frame (the stiff pore is still dry).
- 3) Finally, we apply anisotropic Gassmann’s equations (Gassmann, 1951) to calculate the moduli of the fully saturated model.

The methodologies to calculate the model compliances (step 1), the crack stiffness relaxation function (step 2), and the moduli of the fully saturated model (step 3) are given next.

General expressions

The key result of part 1 (Alkhimenkov and Quintal, 2021) is the general expression to calculate the effective viscoelastic stiffness tensor for any geometry of the pore space using the property contribution tensors. The effective compliance matrix for the dry model represented in Figure 4a can be written as (in Voigt notation)

$$[S_{mn}^*]_{\text{dry}} = S_{mn}^g + [H_{mn}]_{\text{dry}}, \quad (1)$$

where S_{mn}^g is the compliance matrix of the solid grains and $[H_{mn}]_{\text{dry}}$ is the compliance contribution matrix of the dry pore space (a crack connected to a pore or multiple pores). The effective compliance matrix for the modified frame can be calculated as

$$[S_{mn}^*(\omega)]^{\text{MF}} = S_{mn}^g + [H_{mn}^p]_{\text{dry}} + [H'_{mn}(\omega)]^{\text{MF}}, \quad (2)$$

where $[H_{mn}^p]_{\text{dry}}$ is the compliance contribution matrix of the stiff pore(s), $[H'_{mn}(\omega)]^{\text{MF}}$ is the additional compliance contribution matrix due to the presence of a saturated crack connected to a dry pore or multiple dry pores, and ω is the angular frequency; $[H'_{33}(\omega)]^{\text{MF}}$ is the frequency-dependent component with the moduli of the crack stiffness relaxation (given next). Finally, the effective stiffness matrix for the saturated model is calculated as

$$[C_{mn}^*(\omega)]_{\text{sat}} = ([S_{mn}^*(\omega)]^{\text{MF}})^{-1} + [\text{fluid via Gassmann’s equations}], \quad (3)$$

Table 3. Geometric properties for the models with one, two, and four spheres and the big pore model with a crack aspect ratio $\alpha = 0.01$.

Geometric parameter	One sphere	Two spheres	Four spheres	Torus
Flat cylinder (crack) radius b (m)	0.1	0.1	0.1	0.1
Flat cylinder (crack) thickness h (m)	0.002	0.002	0.002	0.002
Crack aspect ratio $\alpha = h/(2b)$	0.01	0.01	0.01	0.01
Radius of sphere $b/2$ (m)	0.05	0.05	0.05	0.05
The volume (crack + pore, interconnected)	$\approx 5.832 \times 10^{-4}$	≈ 0.0011	≈ 0.00214	≈ 0.00145
Total porosity	≈ 0.0182	≈ 0.0344	≈ 0.0669	≈ 0.0454
Crack porosity	≈ 0.002	≈ 0.002	≈ 0.002	≈ 0.002

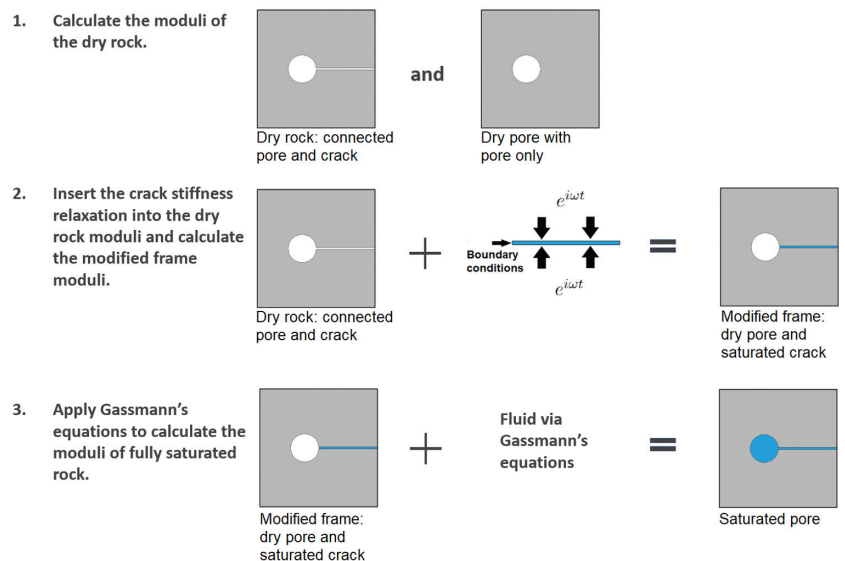


Figure 4. Sketch of the development of the present analytical model.

where [fluid via Gassmann's equations] denotes the application of the anisotropic Gassmann's equations (Gassmann, 1951) to saturate the stiff pore space (pore) with a fluid at each frequency.

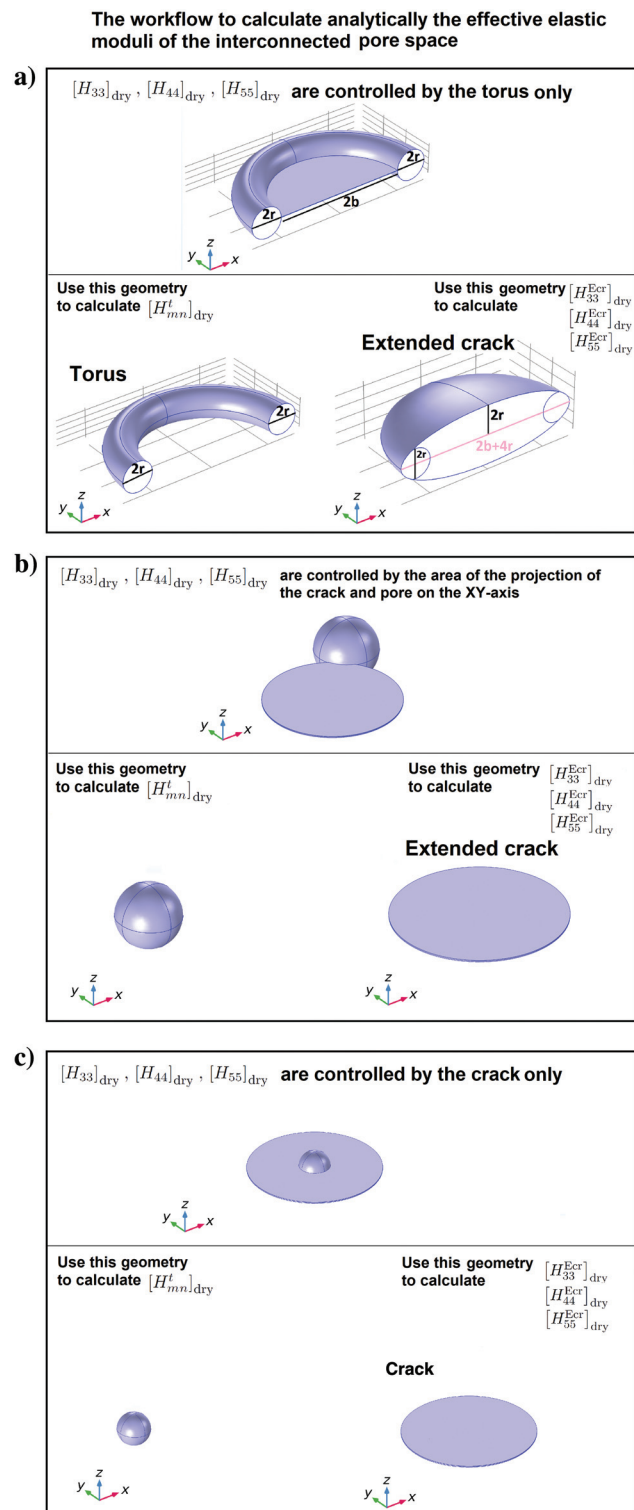


Figure 5. Sketch illustrating the workflow to calculate analytically the stiffness moduli for different configurations of interconnected isometric pores and cracks.

Step 1: Dry model compliances

Figure 5 shows three different geometries of the pore space: a crack fully connected to a torus (Figure 5a), a crack partially connected to a spherical pore (Figure 5b), and a crack with a spherical pore in the center (“Saturn ring”). An analytical approach to calculate the effective compliance matrices of the mentioned dry models is briefly explained next. We exploit the approach used in micro-mechanics to construct the property contribution matrix of complex geometries (e.g., intersecting cracks, inclusions of “irregular” shapes, chapters 4.3 and 4.4 in Kachanov and Sevostianov, 2018). The main idea is that by using 3D numerical simulations for the complex pore space, we find the structure and the symmetry of the compliance contribution matrix, its principal directions, and the key geometric characteristics of the complex pore space which control the compliance of the model. Then, we are able to construct the compliance contribution matrix of the interconnected pore(s) and crack by using the known property contribution tensors for simple geometries (Alkhimenkov and Quintal, 2021).

A crack connected to a torus

The method to calculate the compliance contribution matrices of a dry model with a crack connected to a torus (the same as shown in Figures 2f and 5a) is presented in Alkhimenkov and Quintal (2021). The analytical approach to construct the property contribution matrix for this complex geometry provides us with a very good approximation (validated against accurate numerical solutions). The disadvantage of this geometry is that this model is quite artificial: the components $[H_{33}]_{\text{dry}}, [H_{44}]_{\text{dry}},$ and $[H_{55}]_{\text{dry}}$ are controlled by the torus only, so the crack thickness does not affect the effective properties of the dry model (see Figure 17 in Alkhimenkov and Quintal, 2021). In real rocks, crack density and crack thickness do affect the effective elastic moduli. That is why this widely used classical pore geometry for squirt flow should no be longer used.

A crack with a pore in the center

Another end-member geometry is represented by a crack with a pore in the center (Saturn ring) (Figure 5c). The analytical approach to construct the property contribution matrix for this geometry is given in Kachanov and Sevostianov (2018). In this configuration, the components $[H_{33}]_{\text{dry}}, [H_{44}]_{\text{dry}},$ and $[H_{55}]_{\text{dry}}$ are controlled by the crack only (if the crack radius is at least two times larger than the radius of the sphere). Therefore, the compliance contribution matrix $[H_{mn}]_{\text{dry}}$ (expression 1) is calculated using the expressions for a spherical pore, except for the components $[H_{33}]_{\text{dry}}, [H_{44}]_{\text{dry}},$ and $[H_{55}]_{\text{dry}},$ which are calculated using the expressions for a crack (Figure 5c).

A crack partially connected to a pore or multiple pores

To date, there is no accurate approach to construct the compliance contribution matrices of a crack partially connected to a pore or multiple pores using analytical expressions (Figures 3b–3d and 5b). Here, we provide an approximate solution whose accuracy is lower compared with the two previously mentioned geometries. This approximate solution can be used for the interconnected pore(s) and crack if no precise numerical solution is available.

Our approximate solution is simple: the property contribution matrix can be calculated using only analytical expressions. The general idea is the same as for the pore space geometry consisting of a crack

connected to a torus (Alkhimenkov and Quintal, 2021). For the geometry shown in Figure 5b, the components $[H_{33}]_{dry}$, $[H_{44}]_{dry}$, and $[H_{55}]_{dry}$ are controlled simultaneously by the crack and the sphere. The compliance contribution matrix $[H_{mn}]_{dry}$ (expression 1) is calculated using the expressions for a spherical pore, except for the components $[H_{33}]_{dry}$, $[H_{44}]_{dry}$, and $[H_{55}]_{dry}$, which are calculated using the expressions for the extended crack (Figure 5c). The area of the projection of the crack partially connected to a pore on the xy -axis will define the area of the circular (penny-shaped) extended crack. The thickness of the extended crack can be the same as the thickness of the crack itself. However, if the area of the projection of the pore alone is comparable (or larger) than the area of the projection of the crack alone, then the thickness of the extended crack should be increased. For this case, the appropriate dimensions of the extended crack will be investigated in the future.

One can see that the extended crack radius (Figure 5b) is larger than the radius of the initial crack of the model. As a result, the compliance contribution matrix of a crack partially connected to a pore $[H_{mn}]_{dry}$ is constructed by using the obtained components of a pore $[H_{mn}^p]_{dry}$ and an extended crack $[H_{mn}^{Ecr}]_{dry}$:

$$[H_{mn}]_{dry} = 2 \begin{bmatrix} [H_{11}^p]_{dry} & [H_{12}^p]_{dry} & [H_{13}^p]_{dry} & 0 & 0 & 0 \\ [H_{21}^p]_{dry} & [H_{22}^p]_{dry} & [H_{23}^p]_{dry} & 0 & 0 & 0 \\ [H_{31}^p]_{dry} & [H_{32}^p]_{dry} & [H_{33}^{Ecr}]_{dry} & 0 & 0 & 0 \\ 0 & 0 & 0 & [H_{44}^{Ecr}]_{dry} & 0 & 0 \\ 0 & 0 & 0 & 0 & [H_{55}^{Ecr}]_{dry} & 0 \\ 0 & 0 & 0 & 0 & 0 & [H_{66}^p]_{dry} \end{bmatrix}. \quad (4)$$

The compliance contribution matrix of the modified frame is

$$[H_{mn}(\omega)]^{MF} = 2 \begin{bmatrix} [H_{11}^p]_{dry} & [H_{12}^p]_{dry} & [H_{13}^p]_{dry} & 0 & 0 & 0 \\ [H_{21}^p]_{dry} & [H_{22}^p]_{dry} & [H_{23}^p]_{dry} & 0 & 0 & 0 \\ [H_{31}^p]_{dry} & [H_{32}^p]_{dry} & [H_{33}^{Ecr}(\omega)]^{MF} & 0 & 0 & 0 \\ 0 & 0 & 0 & [H_{44}^{Ecr}]_{dry} & 0 & 0 \\ 0 & 0 & 0 & 0 & [H_{55}^{Ecr}]_{dry} & 0 \\ 0 & 0 & 0 & 0 & 0 & [H_{66}^p]_{dry} \end{bmatrix}, \quad (5)$$

where a new component $[H_{33}^{Ecr}(\omega)]^{MF}$ is introduced (analogous to the classical geometry presented in Alkhimenkov and Quintal, 2021). Fluid flow takes place in the crack in one plane; therefore, the relaxation of the crack compliance is denoted by only the $[H_{33}^{Ecr}(\omega)]^{MF}$ component. The expression for the $[H_{33}^{Ecr}(\omega)]^{MF}$ is given next.

To separate the compliance contribution of a pore, which is a constant value across all frequencies, from the contribution of the extended crack compliance, which is frequency dependent, we introduce (Alkhimenkov and Quintal, 2021)

$$[H'_{mn}(\omega)]^{MF} = [H_{mn}(\omega)]^{MF} - [H_{mn}^{ip}]_{dry}$$

$$= 2 \begin{bmatrix} 0 & 0 & 0 & 0 & 0 & 0 \\ 0 & 0 & 0 & 0 & 0 & 0 \\ 0 & 0 & [H'_{33}(\omega)]^{MF} & 0 & 0 & 0 \\ 0 & 0 & 0 & [H'_{44}]_{dry}^{MF} & 0 & 0 \\ 0 & 0 & 0 & 0 & [H'_{55}]_{dry}^{MF} & 0 \\ 0 & 0 & 0 & 0 & 0 & 0 \end{bmatrix}. \quad (6)$$

The structure of the compliance contribution matrix (equation 6) is the same as the compliance contribution matrix of a crack embedded into a homogeneous elastic material (Schoenberg and Douma, 1988; Schoenberg and Helbig, 1997). (The crack compliance can be written in terms of normal and tangential compliances.) However, the absolute values of its components are completely different compared with the values obtained for a crack embedded into a homogeneous elastic material (Alkhimenkov and Quintal, 2021). Note that

$$\lim_{\omega \rightarrow +0} [H'_{33}(\omega)]^{MF} = [H_{33}^{Ecr}]_{dry} - [H_{33}^p]_{dry} \equiv Z_n^{Ap}, \quad (7)$$

where for simplicity we introduce the apparent normal crack compliance Z_n^{Ap} . The apparent tangential crack compliance is $Z_t^{Ap} = [H'_{44}]_{dry}^{MF} \equiv [H'_{55}]_{dry}^{MF}$.

If there are several pores (Figure 3b and 3c), the approach is still the same. If the area of the stiff pores (not including the crack) projected into the XY -plane is comparable or larger than the area of the crack alone, then the thickness of the extended crack can be increased to make the model softer in $[H_{33}]_{dry}$, $[H_{44}]_{dry}$, and $[H_{55}]_{dry}$ components.

Frequency-dependent crack stiffness

The derivation of the frequency-dependent normal component $[H'_{33}(\omega)]^{MF}$ of the modified frame contribution matrix is provided in Alkhimenkov and Quintal (2021). (Maple script also is provided to reproduce and extend the derivation.) In this derivation, the anisotropic Gassmann's equations are used to calculate the moduli considering the crack as being saturated, given that the compliance contribution matrix of the thin crack is described by two parameters only (see expression 7). Here, we directly report the resulting expression (Alkhimenkov and Quintal, 2021),

$$[H'_{33}(\omega)]^{MF} = \frac{(K_g - K_f^*(\omega))\phi_c Z_n^{Ap}}{(K_g - K_f^*(\omega))\phi_c + K_f^*(\omega)K_g Z_n^{Ap}}, \quad (8)$$

where ϕ_c is the compliant porosity (crack porosity), Z_n^{Ap} is the normal apparent compliance of the crack, $K_f^*(\omega)$ is the frequency-dependent fluid bulk modulus, and K_g is the bulk modulus of the solid grains. The apparent tangential crack compliance is $Z_t^{Ap} = [H'_{44}]_{dry}^{MF} \equiv [H'_{55}]_{dry}^{MF}$. If the frequency of the applied strain boundary conditions is low, then the crack is in a relaxed state and

$$[H'_{33}(0+)]^{MF} = Z_n^{Ap}. \quad (9)$$

If the frequency is high, then the crack is in an unrelaxed state and

$$[H'_{33}(+\infty)]^{MF} = 0. \quad (10)$$

The full expression to calculate $K_f^*(\omega)$ is given in the next section.

Extension for cracks with finite thickness

Here, we repeat the method presented by Alkhimenkov and Quintal (2021) to calculate the normal apparent crack compliance for a crack with a finite thickness. If the crack thickness is not so small (i.e., if the aspect ratio is larger 0.0025), then the expression 10 is not equal to zero. A small nonzero value of Z_n^{th} will be present:

$$\lim_{\omega \rightarrow +\infty} [H'_{33}(\omega)]^{\text{MF}} = [Z_n^{\text{AP}}]^{f\text{th}}. \quad (11)$$

The normal apparent crack compliance becomes

$$[Z_n^{\text{AP}}]^f = Z_n^{\text{AP}} - [Z_n^{\text{AP}}]^{f\text{th}}. \quad (12)$$

The only modification that is needed is a slight change in expression 8 by including the additional compliance $[Z_n^{\text{AP}}]^{f\text{th}}$:

$$[H'_{33}]^{\text{MF}} = \frac{(K_g - K_f^*(\omega))\phi_c [Z_n^{\text{AP}}]^f}{(K_g - K_f^*(\omega))\phi_c + K_f^*(\omega)K_g[Z_n^{\text{AP}}]^f} + [Z_n^{\text{AP}}]^{f\text{th}}. \quad (13)$$

Step 2: Relaxation of the crack stiffness

Fluid pressure diffusion behavior in the crack strongly depends on the portion of the crack circumference connected to the stiff pore as shown in Figures 2 and 3. Furthermore, high fluid pressure anomalies in the regions close to the connected stiff pores dramatically change the shape of the attenuation curve $1/Q$ (Figures 2h and 3f). The characteristic frequency also is different for different pore geometries even though the crack aspect ratio stays the same (Figures 2h and 3f). All of these observations obtained from the 3D numerical solutions allow us to revise the previous qualitative and quantitative description of the squirt flow physics. By analyzing the numerical results (Figures 2 and 3), we find that the characteristic frequency is different for radial and approximately 1D fluid pressure diffusion. Then, we analyze analytical solutions for the fluid pressure considering radial and 1D fluid pressure diffusion; we find out that the solutions for crack stiffness considering 1D fluid pressure diffusion provide us with an excellent approximation for pore space geometries presented in the present study. Next, we provide a new expression for the crack stiffness relaxation function. Only if the pore space geometry uses radial fluid pressure diffusion (big pore and 8/9 torus geometries), expressions for radial fluid pressure diffusion should be used. (They are presented in Appendix A). We also revise the parameters which control the characteristic frequency of squirt flow.

Fluid pressure diffusion in a layer

For a 1D configuration, we assume that fluid flow takes place in the x -direction in an infinite-strip layer (i.e., infinite length in the

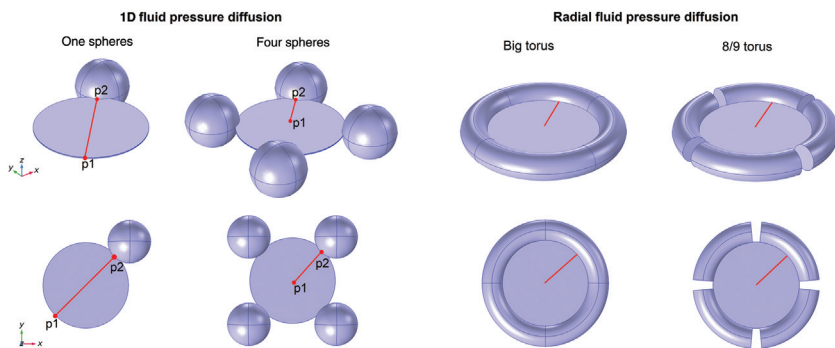


Figure 6. Sketch illustrating the definition of the squirt flow length l_{sq} for different geometries.

y -direction); l^{sq} and h^{sq} are the width and thickness of the layer, respectively. We set the following boundary conditions: the compression sinusoidal strain ϵ_c as a function of frequency is applied to the walls of the layer and the zero fluid pressure is applied at the edge of the layer (see step 2 in Figure 4 for the 1D layer configuration and applied boundary conditions). The solution for the fluid pressure p in the layer is frequency dependent. The 1D version of equation 23 in Alkhimenkov and Quintal (2021) for the fluid pressure can be written as

$$\frac{\partial^2 p}{\partial x^2} - k^2 p = -k^2 K_f \epsilon_c, \quad (14)$$

where

$$k = \frac{2}{h} \sqrt{3i\omega\eta / (K_f + \frac{4}{3}i\omega\eta)} \quad (15)$$

is a function of the rheology of the layer (e.g., Tsai and Lee, 1998) and K_f is the fluid bulk modulus. For the derivation of the solution 14 with zero stress at the $x = l^{\text{sq}}$ boundary condition, we use the elastic-viscoelastic correspondence principle (Hashin, 1970). A full derivation is available in a permanent repository (Maple script and a PDF with derivations). The resulting solution is

$$K_f^*(\omega) = K_f + \frac{4}{3}i\omega\eta - \frac{(K_f - \frac{2}{3}i\omega\eta)^2 \tanh(\bar{k}_3)}{(K_f + \frac{4}{3}i\omega\eta) \bar{k}_3}, \quad (16)$$

where η is the fluid shear viscosity and

$$\bar{k}_3 = \frac{1}{\alpha} \sqrt{3i\omega\eta / (K_f + \frac{4}{3}i\omega\eta)}. \quad (17)$$

Note that solution 16 is the same as presented by Tsai and Lee (1998).

The squirt flow aspect ratio α^{sq}

The squirt flow length l^{sq} is the distance between the two points p1 and p2; p1 is the most distant point (p1) in the crack from the pore(s) and p2 is the point where crack is connected to a pore (see Figure 6). The squirt flow thickness h^{sq} is the crack aperture. For realistic cracks, the aperture varies due to asperities, so the minimum value of the aperture of the crack should be used (Lissa et al., 2020). Finally, the parameter controlling the characteristic frequency is the squirt flow aspect ratio α^{sq} :

$$\alpha^{\text{sq}} = \frac{1}{2} \frac{h^{\text{sq}}}{l^{\text{sq}}}. \quad (18)$$

Figure 6 illustrates the definition of the squirt flow length parameter l_{sq} for different geometries. For models with one sphere and four spheres, the expressions 16 (i.e., 1D fluid pressure diffusion) and 8 for the crack stiffness relaxation should be used. Note that the squirt flow length in the model with one sphere is twice that in the model with four spheres (because l^{sq} is the distance between the two points p1 and p2 [Figure 6]). For

the big torus or 8/9 torus models, the expressions A-1 and 8 should be used because the fluid pressure diffusion is mostly radial. The characteristic frequency in the case of 1D fluid pressure diffusion (expression 16) is at slightly lower frequencies compared with the case of the radial fluid pressure diffusion for the exact same squirt flow length l_{sq} . If the crack has finite thickness, then the expression 13 should be used instead of the expression 8.

Step 3: Stiffness of the fully saturated model

Once the effective compliance matrix for the modified frame is calculated using the expression 2, we saturate the modified frame moduli with a fluid at each frequency using anisotropic Gassmann’s equations (Gassmann, 1951) (see expression 3):

$$[C_{mn}^*(\omega)]_{sat} = ([S_{mn}^*(\omega)]^{MF})^{-1} + \alpha_m \alpha_n M, \quad (19)$$

$$\alpha_m = 1 - \left(\sum_{n=1}^3 C_{mn}^{MF} \right) / K_g / 3, \quad (20)$$

for $m = 1, 2, 3$ and $\alpha_4 = \alpha_5 = \alpha_6 = 0$, and where

$$M = (\phi / K_f + (1 - \phi) / K_g - K^* / K_g^2)^{-1}, \quad (21)$$

$$K^* = \frac{1}{9} \sum_{m=1}^3 \sum_{n=1}^3 C_{mn}^{MF}(\omega), \quad (22)$$

where ϕ is the total porosity of the rock without the compliant porosity (which is neglected because it is usually two or more orders of magnitude lower than the stiff pore’s porosity), K^* is the generalized bulk modulus of the modified frame, and α_m is the Biot-Willis coefficient.

NUMERICAL VALIDATION OF THE ANALYTICAL MODEL

Figure 7 shows results for the real part of the $[C_{33}^*(\omega)]_{sat}$ complex-valued component of the stiffness matrix for the big pore model obtained with the present analytical model, the standard linear solid model (equation 50 in Alkhimenkov and Quintal, 2021), the modified model of Collet and Gurevich (2016) (model B, with correct limits), the approximation of the modified model of Collet and Gurevich (2016) (model B), and the numerical solution. The modified model of Collet and Gurevich (2016) is presented in Appendix B of Alkhimenkov and Quintal (2021).

Figure 8 shows results for the real part of the complex-valued component of the stiffness matrix for the big pore model and the models with one sphere and four spheres. Our analytical models are in good agreement with numerical solutions confirming that they can adequately and accurately describe the frequency-dependent stiffness and attenuation associated with squirt flow. We provide MATLAB routines to reproduce Figures 7 and 8 in the “Data and materials availability” section.

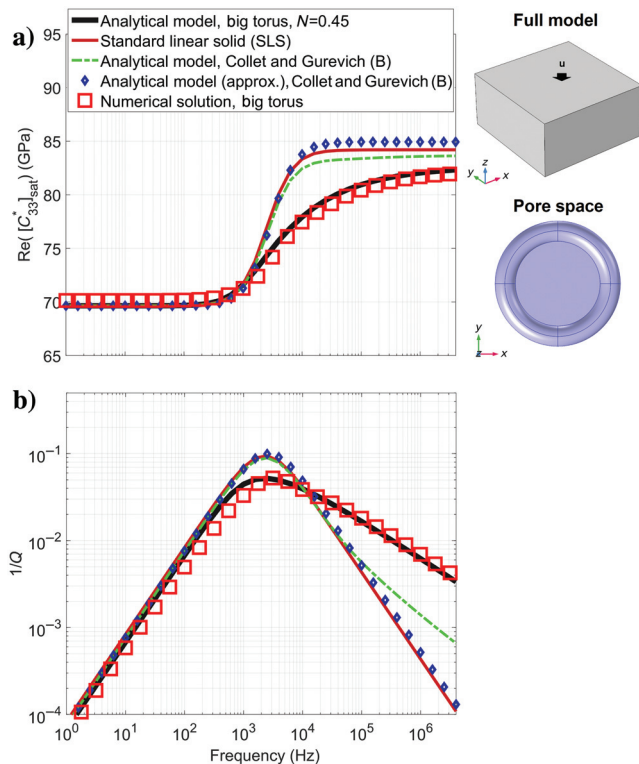


Figure 7. Numerical and analytical results for the big pore model. The crack aspect ratio is $\alpha = 0.005$. (a) Real part of the stiffness component and (b) corresponding dimensionless attenuation. On the right, the geometry of the pore space is shown. N is a parameter used for the branching function and this is explained in Appendix A.

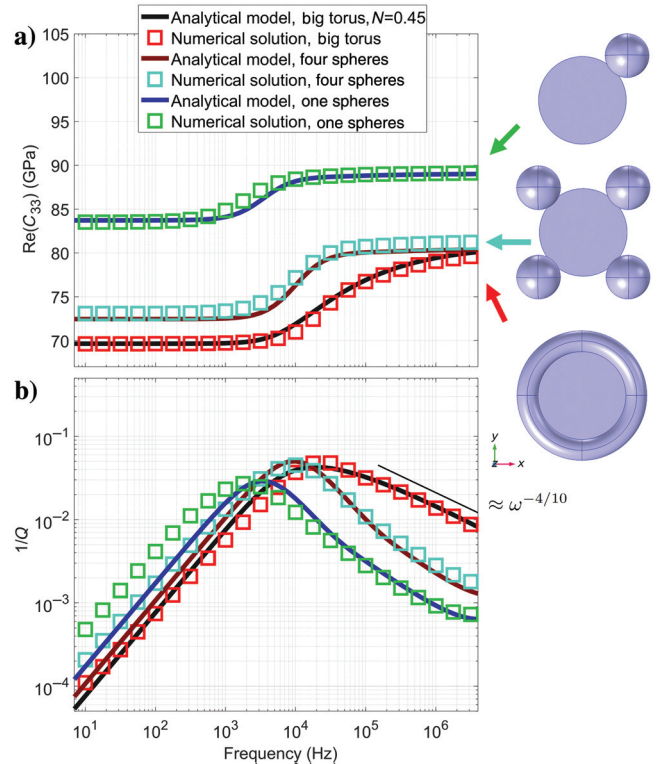


Figure 8. Numerical and analytical results for the big pore model and the models with four spheres and one sphere. The crack aspect ratio is $\alpha = 0.01$. (a) Real part of the stiffness component and (b) corresponding dimensionless attenuation. On the right, geometries of the pore space are shown.

DISCUSSION

Do we need a distribution of crack aspect ratios for a smooth transition?

Figure 9 shows results for the real part of the $[C_{33}^*(\omega)]_{\text{sat}}$ complex-valued component of the stiffness matrix for the big pore model, the big pore model incorporating a sphere in the center, and the crack with the sphere in the center. These results show that even a single crack interconnected to one or several pores can produce very smooth transition from low to high frequencies of $1/Q$. (The critical frequency is spread over some intervals.)

The characteristic frequency

Although the geometric crack aspect ratio is kept constant, the effective crack aspect ratio may increase if the fluid path length decreases. We conclude that a key factor controlling the characteristic frequency is a parameter that we call here the squirt flow length, which corresponds to a 1D fluid pressure diffusion path in the considered models. This parameter describes well the characteristic frequency and is related to the crack length, and the number of connections to other pores. For a more accurate description of the characteristic frequency as a function of these geometric characteristics of the pore space, a systematic analysis will be carried out in the future.

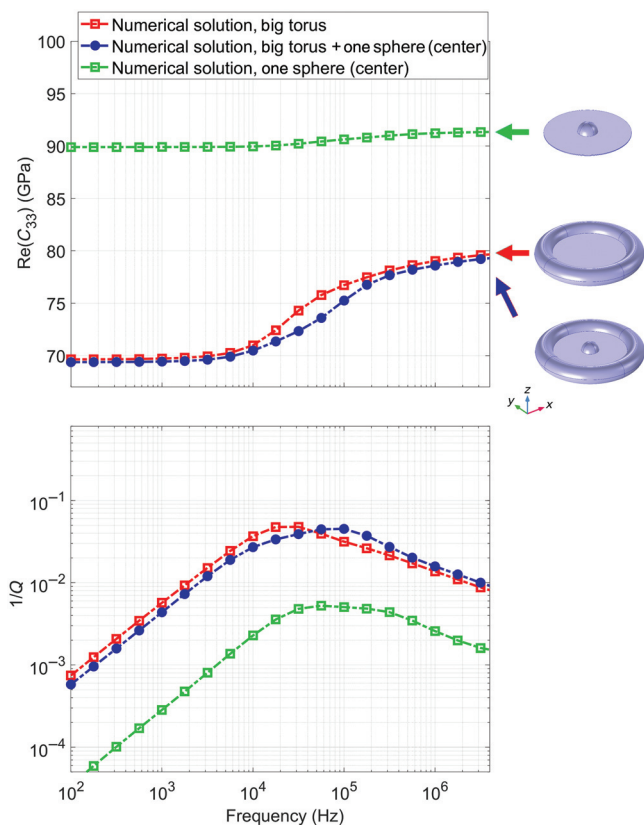


Figure 9. Numerical results for the big pore model, the big pore model incorporating a sphere in the center, and the crack with the sphere in the center. The crack aspect ratio is $\alpha = 0.01$. (a) Real part of the stiffness component and (b) corresponding dimensionless attenuation. On the right, the geometries of the pore space are shown.

Applicability of the classical pore geometry

To date, most of the analytical models trying to quantitatively model seismic dispersion and attenuation are based on the classical geometry: a crack interconnected to a toroidal pore (Dvorkin et al., 1995; Gurevich et al., 2010; Alkhimenkov and Quintal, 2021). However, this pore geometry cannot be used to represent the pore space of a rock due to a specific reason. The stiffness of a porous rock (where cracks can be represented by grain-to-grain contacts) can be parameterized by three components (for simplicity): a rock matrix, pores, and cracks. Generally speaking, the more pores, the softer the rock. At the same time, the more cracks, the softer the rock. As a result, the pores and cracks independently control the rock stiffness. However, the rock model represented by a crack interconnected to a toroidal pore does not support this. Alkhimenkov and Quintal (2021) show that the stiffness of a such model is mainly controlled by the toroidal pore; if the crack thickness is increased by a factor of 50, the resulting stiffness will stay the same. Therefore, this model should no longer be used. Another disadvantage of this geometry is that the accurate description of seismic dispersion and attenuation requires cumbersome expressions, which are difficult to analyze (Appendix A).

Instead, we present another rock model where a crack is partially connected to several pores; in such configuration, the rock stiffness is independently controlled by the contributions of a crack and pores, which is in agreement with the observation from real rocks. Furthermore, the resulting analytical expressions of seismic dispersion and attenuation are very simple and include only algebraic operations and one trigonometric function. Nevertheless, this new analytical model is in good agreement with the 3D numerical solution for the exact same geometry.

Analytical model for isotropic rocks

The results presented in this paper can be directly applied to model seismic attenuation and dispersion caused by squirt flow in fluid-saturated isotropic rocks. A viscoelastic response of a fluid-saturated isotropic rock can be described by the two parameters, bulk $K_{\text{sat}}(\omega)$ and shear $\mu_{\text{sat}}(\omega)$ moduli. The expressions for the unrelaxed moduli of a fluid-saturated isotropic rock (K_{uf} and μ_{uf}) can be found in Mavko and Jizba (1991) (expression 10 for K_{uf} and expression 22 for μ_{uf}). Or, as an alternative, expression 5 for K_{uf} from Gurevich et al. (2010) can be used. In the expressions for K_{uf} and μ_{uf} , one can replace the fluid bulk modulus with the viscoelastic relaxation function presented in this study (expression 16). The resulting expressions are, in fact, the moduli of the modified frame as a function of frequency ($K_{mf}(\omega)$ and $\mu_{mf}(\omega)$). Then, one can saturate the modified frame moduli with a fluid at each frequency using isotropic Gassmann's equations (Gassmann, 1951). As a result, bulk $K_{\text{sat}}(\omega)$ and shear $\mu_{\text{sat}}(\omega)$ moduli of a fully saturated rock are derived. In this model, the characteristic frequency is controlled by the squirt flow aspect ratio α^{sq} (expression 18). This isotropic model still requires further validation against 3D numerical solutions.

CONCLUSION

We have extended the analytical model for seismic dispersion and attenuation caused by squirt flow that was presented in part 1 to more complex geometries of the pore space, where the crack is partially connected to one or multiple spherical pores. This geometry

is much more closely representative of a rock pore space geometry than the classical geometry where the crack edge is fully connected to a toroidal pore. Our analytical model is in good agreement with accurate 3D numerical simulations for a range of different geometries of the pore space. In our analytical model, we provide a general approach to calculate the elastic moduli of interconnected crack and pores. Even though this approach is an approximation, the result is much more accurate compared with previously published solutions where the interconnectivity of cracks and pores is ignored in the calculation of the model compliances. We also provide a good approximation for the relaxation of the crack stiffness due to fluid pressure diffusion, which makes our model accurate for the whole frequency band for different geometries. We observe that the key factor controlling the characteristic frequency is the squirt flow aspect ratio, which is the ratio between the squirt flow thickness and two times the squirt flow length, where the latter corresponds to a 1D fluid pressure diffusion path that can be different in the considered models, and not simply to the crack length as in the classic model of a crack connected to a toroidal pore. More precisely, the squirt flow length is the length between the point in the crack at the maximum distance from all pores and the point where the crack edge is connected to a pore. The squirt flow thickness is equal to the crack aperture if this one is constant. This study redefines the quantitative and qualitative description of seismic attenuation and velocity dispersion due to squirt flow.

ACKNOWLEDGMENTS

This research is funded by the Swiss National Science Foundation, project number 172691. Y. Alkhimenkov thanks the reviewers B. Gurevich and Y. Guéguen for many valuable suggestions. The authors thank P. Logean for technical support.

DATA AND MATERIALS AVAILABILITY

No data were used in producing this manuscript. The routines archive (v1.0) is available from a permanent DOI repository (Zenodo) at <http://doi.org/10.5281/zenodo.6974394> (Alkhimenkov and Quintal, 2021).

APPENDIX A

RADIAL FLUID PRESSURE DIFFUSION IN A CRACK

Fluid pressure diffusion in a penny-shaped crack due to the applied strain to the walls of the crack can be radial. For such a configuration, the solutions are given by Murphy et al. (1986) for a boundary condition to the crack edge taking into account a finite volume of the pore, and the solutions are given by Chalhoub and Kelly (1990) and Tsai and Lee (1998) for zero fluid pressure boundary condition to the crack edge. However, if the sinusoidal strain is applied to the walls of the full model consisting of a crack connected to a torus and embedded into a solid material, the resulting fluid pressure diffusion in a crack is different due to the presence of the torus (high pressure “ring anomaly” in Figure 2f). Alkhimenkov and Quintal (2021) propose an approximation to the relaxation of the fluid pressure for the classical geometry by using the solution for a crack from Murphy et al. (1986), Chalhoub and Kelly (1990), and Tsai and Lee (1998) with a modified high-frequency asymptote. Our numerical analysis for a pore represented by fractions of a torus

(Figure 2b–2f) shows that the high-frequency asymptote is different for models with different fractions of a torus. In the present study, we extend and improve the solution of Alkhimenkov and Quintal (2021) to include the models having a crack connected to fractions of a torus (Figure 2b–2f). We approximate the solution for crack stiffness relaxation via the frequency-dependent fluid bulk modulus $K_f^*(\omega)$ using the following branching function:

$$K_f^*(\omega) = K_f - (K_f - y \cdot K_f^{LF}) / [1 - \zeta + \zeta(1 + i\omega\tau/\zeta^2)^N], \tag{A-1}$$

where $y = 0$ for the solution considering zero fluid pressure at the crack tip or $y = 1$ for the solution considering nonzero fluid pressure boundary condition at the crack tip. The parameter N denotes the slope of the high-frequency asymptote $1/Q$ of the fluid bulk $K_f^*(\omega)$ relaxation. If $N = 0.5$, then the expression A-1 reduces to the expression 33 from Alkhimenkov and Quintal (2021), which is approximately valid for a toroidal pore. If $N \neq 0.5$, then the high-frequency asymptote of $K_f^*(\omega)$ relaxation is different; N is a function of the fraction of the crack circumference which is connected to a (few) pore(s). A better result for a toroidal pore is achieved by taking $N = 0.45$, resulting in the slope of the $1/Q$ high-frequency asymptote of $\approx \omega^{-4.5/10}$ (Figures 7 and 8). For 8/9 torus model, $N = 0.55$, resulting in the slope of the $1/Q$ high-frequency asymptote of $\approx \omega^{-4.5/10}$ (Figure A-1). If $N > 0.55$, then the resulting slope is $> \omega^{-4.5/10}$. However, already for 6/9 torus model, the characteristic frequency shifts to lower frequencies and the expression 16 for a 1D fluid pressure diffusion should be used.

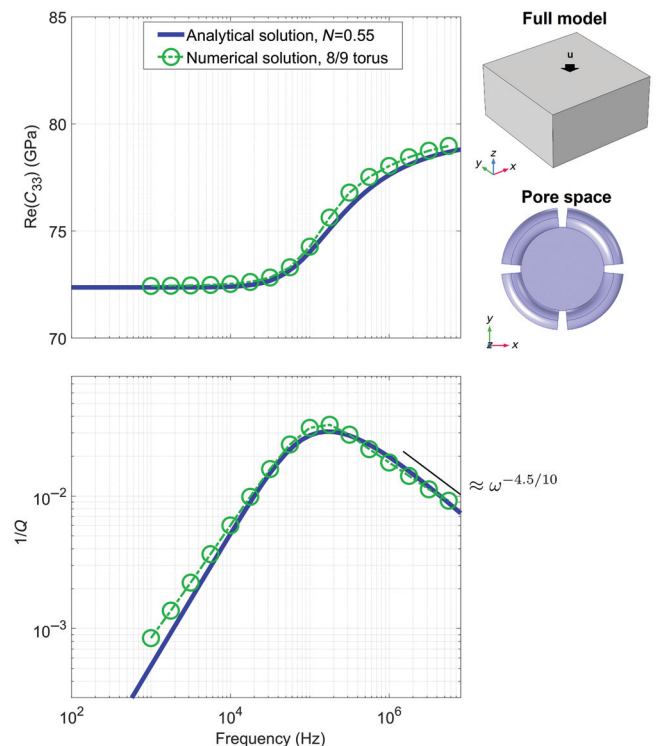


Figure A-1. Numerical and analytical results for the 8/9 torus model: (a) Real part of the stiffness component and (b) corresponding dimensionless attenuation. On the right, geometries of the pore space are shown.

Downloaded 10/07/22 to 185.25.195.104. Redistribution subject to SEG license or copyright; see Terms of Use at http://library.seg.org/page/policies/terms DOI: 10.1190/geo2022-0143.1

We have derived the expressions for ζ and τ analytically using the Maple symbolic environment. The resulting expressions are simple but cumbersome; they are given in material listed in the “Data and materials availability” section (MATLAB and Maple scripts, a PDF with a derivation). The characteristic frequency of $K_f^*(\omega)$ in the crack is

$$f_c^{\text{crack}} = \frac{4}{\sqrt{3}} \frac{\sqrt{K_f K_f^{\text{LF}}}}{\eta} \alpha^2. \quad (\text{A-2})$$

The apparent fluid bulk modulus at low frequencies K_f^{LF} is

$$K_f^{\text{LF}} = \frac{V_{cr} K_f}{V_{cr} + V_{por}}. \quad (\text{A-3})$$

A more accurate (and more cumbersome) expression for K_f^{LF} also is provided in material listed in the “Data and materials availability” section.

REFERENCES

- Alkhimenkov, Y., E. Caspari, B. Gurevich, N. D. Barbosa, S. Glubokovskikh, J. Hunziker, and B. Quintal, 2020a, Frequency-dependent attenuation and dispersion caused by squirt flow: Three-dimensional numerical study: *Geophysics*, **85**, no. 3, MR129–MR145, doi: [10.1190/geo2019-0519.1](https://doi.org/10.1190/geo2019-0519.1).
- Alkhimenkov, Y., E. Caspari, S. Lissa, and B. Quintal, 2020b, Azimuth-, angle- and frequency-dependent seismic velocities of cracked rocks due to squirt flow: *Solid Earth*, **11**, 855–871, doi: [10.5194/se-11-855-2020](https://doi.org/10.5194/se-11-855-2020).
- Alkhimenkov, Y., and B. Quintal, 2021, An accurate analytical model for squirt flow in anisotropic porous rocks — Part I: Classical geometry: *Geophysics*, **87**, no. 2, MR85–MR103, doi: [10.1190/geo2021-0229.1](https://doi.org/10.1190/geo2021-0229.1).
- Chalhoub, M. S., and J. M. Kelly, 1990, Effect of bulk compressibility on the stiffness of cylindrical base isolation bearings: *International Journal of Solids and Structures*, **26**, 743–760, doi: [10.1016/0020-7683\(90\)90004-F](https://doi.org/10.1016/0020-7683(90)90004-F).
- Chapman, M., 2003, Frequency-dependent anisotropy due to meso-scale fractures in the presence of equant porosity: *Geophysical Prospecting*, **51**, 369–379, doi: [10.1046/j.1365-2478.2003.00384.x](https://doi.org/10.1046/j.1365-2478.2003.00384.x).
- Chapman, M., S. V. Zatsepin, and S. Crampin, 2002, Derivation of a micro-structural poroelastic model: *Geophysical Journal International*, **151**, 427–451, doi: [10.1046/j.1365-246X.2002.01769.x](https://doi.org/10.1046/j.1365-246X.2002.01769.x).
- Collet, O., and B. Gurevich, 2016, Frequency dependence of anisotropy in fluid saturated rocks — Part I: Aligned cracks case: *Geophysical Prospecting*, **64**, 1067–1084, doi: [10.1111/1365-2478.12384](https://doi.org/10.1111/1365-2478.12384).
- Das, V., T. Mukerji, and G. Mavko, 2019, Numerical simulation of coupled fluid-solid interaction at the pore scale: A digital rock-physics technology: *Geophysics*, **84**, no. 4, WA71–WA81, doi: [10.1190/geo2018-0488.1](https://doi.org/10.1190/geo2018-0488.1).
- Dvorkin, J., G. Mavko, and A. Nur, 1995, Squirt flow in fully saturated rocks: *Geophysics*, **60**, 97–107, doi: [10.1190/1.1443767](https://doi.org/10.1190/1.1443767).
- Gassmann, F., 1951, Über die Elastosis poroser Medien: *Vierteljahrsschrift der Naturforschenden Gesellschaft in Zurich*, **96**, 1–23.
- Gurevich, B., D. Makarynska, O. B. de Paula, and M. Pervukhina, 2010, A simple model for squirt-flow dispersion and attenuation in fluid-saturated granular rocks: *Geophysics*, **75**, no. 6, N109–N120, doi: [10.1190/1.3509782](https://doi.org/10.1190/1.3509782).
- Hashin, Z., 1970, Complex moduli of viscoelastic composites — I. General theory and application to particulate composites: *International Journal of Solids and Structures*, **6**, 539–552, doi: [10.1016/0020-7683\(70\)90029-6](https://doi.org/10.1016/0020-7683(70)90029-6).
- Jakobsen, M., and M. Chapman, 2009, Unified theory of global flow and squirt flow in cracked porous media: *Geophysics*, **74**, no. 2, WA65–WA76, doi: [10.1190/1.3078404](https://doi.org/10.1190/1.3078404).
- Kachanov, M., and I. Sevostianov, 2018, *Micromechanics of materials, with applications*: Springer 249.
- Lissa, S., N. D. Barbosa, E. Campari, Y. Alkhimenkov, and B. Quintal, 2020, Squirt flow in cracks with rough walls: *Journal of Geophysical Research: Solid Earth*, **125**, e2019JB019235, doi: [10.1029/2019JB019235](https://doi.org/10.1029/2019JB019235).
- Lissa, S., M. Ruf, H. Steeb, and B. Quintal, 2021, Digital rock physics applied to squirt flow: *Geophysics*, **86**, no. 4, MR235–MR245, doi: [10.1190/geo2020-0731.1](https://doi.org/10.1190/geo2020-0731.1).
- Mavko, G., and D. Jizba, 1991, Estimating grain-scale fluid effects on velocity dispersion in rocks: *Geophysics*, **56**, 1940–1949, doi: [10.1190/1.1443005](https://doi.org/10.1190/1.1443005).
- Mavko, G., and A. Nur, 1975, Melt squirt in the asthenosphere: *Journal of Geophysical Research*, **80**, 1444–1448, doi: [10.1029/JB080i01p01444](https://doi.org/10.1029/JB080i01p01444).
- Mukerji, T., and G. Mavko, 1994, Pore fluid effects on seismic velocity in anisotropic rocks: *Geophysics*, **59**, 233–244, doi: [10.1190/1.1443585](https://doi.org/10.1190/1.1443585).
- Müller, T. M., B. Gurevich, and M. Lebedev, 2010, Seismic wave attenuation and dispersion resulting from wave-induced flow in porous rocks — A review: *Geophysics*, **75**, no. 5, 75A147–75A164, doi: [10.1190/1.3463417](https://doi.org/10.1190/1.3463417).
- Murphy, W. F., K. W. Winkler, and R. L. Kleinberg, 1986, Acoustic relaxation in sedimentary rocks: Dependence on grain contacts and fluid saturation: *Geophysics*, **51**, 757–766, doi: [10.1190/1.1442128](https://doi.org/10.1190/1.1442128).
- O’Connell, R. J., and B. Budiansky, 1977, Viscoelastic properties of fluid-saturated cracked solids: *Journal of Geophysical Research*, **82**, 5719–5735, doi: [10.1029/JB082i036p05719](https://doi.org/10.1029/JB082i036p05719).
- Palmer, I., and M. Traviolia, 1980, Attenuation by squirt flow in undersaturated gas sands: *Geophysics*, **45**, 1780–1792, doi: [10.1190/1.1441065](https://doi.org/10.1190/1.1441065).
- Pride, S. R., J. G. Berryman, and J. M. Harris, 2004, Seismic attenuation due to wave-induced flow: *Journal of Geophysical Research: Solid Earth*, **109**, B01201, doi: [10.1029/2003JB002639](https://doi.org/10.1029/2003JB002639).
- Quintal, B., E. Caspari, K. Holliger, and H. Steel, 2019, Numerically quantifying energy loss caused by squirt flow: *Geophysical Prospecting*, **67**, 2196–2212, doi: [10.1111/1365-2478.12832](https://doi.org/10.1111/1365-2478.12832).
- Quintal, B., J. G. Rubino, E. Caspari, and K. Holliger, 2016, A simple hydro-mechanical approach for simulating squirt-type flow: *Geophysics*, **81**, no. 4, D335–D344, doi: [10.1190/geo2015-0383.1](https://doi.org/10.1190/geo2015-0383.1).
- Schoenberg, M., and J. Douma, 1988, Elastic wave propagation in media with parallel fractures and aligned cracks: *Geophysical Prospecting*, **36**, 571–590, doi: [10.1111/j.1365-2478.1988.tb02181.x](https://doi.org/10.1111/j.1365-2478.1988.tb02181.x).
- Schoenberg, M., and K. Helbig, 1997, Orthorhombic media: Modeling elastic wave behavior in a vertically fractured earth: *Geophysics*, **62**, 1954–1974, doi: [10.1190/1.1444297](https://doi.org/10.1190/1.1444297).
- Tsai, H.-C., and C.-C. Lee, 1998, Compressive stiffness of elastic layers bonded between rigid plates: *International Journal of Solids and Structures*, **35**, 3053–3069, doi: [10.1016/S0020-7683\(97\)00355-7](https://doi.org/10.1016/S0020-7683(97)00355-7).
- Xu, S., 1998, Modelling the effect of fluid communication on velocities in anisotropic porous rocks: *International Journal of Solids and Structures*, **35**, 4685–4707, doi: [10.1016/S0020-7683\(98\)00090-0](https://doi.org/10.1016/S0020-7683(98)00090-0).
- Zhang, Y., L. Song, M. Deffenbaugh, and M. N. Toksoz, 2010, A finite difference method for a coupled model of wave propagation in poroelastic materials: *The Journal of the Acoustical Society of America*, **127**, 2847–2855, doi: [10.1121/1.3372640](https://doi.org/10.1121/1.3372640).
- Zhang, Y., and M. N. Toksoz, 2012, Computation of dynamic seismic responses to viscous fluid of digitized three-dimensional Berea sandstones with a coupled finite-difference method: *The Journal of the Acoustical Society of America*, **132**, 630–640, doi: [10.1121/1.4733545](https://doi.org/10.1121/1.4733545).

Biographies and photographs of the authors are not available.